Broadband Circularly Polarized Implantable Antenna Loaded with Open Slots for Biomedical Applications

Leyuan Li, Guolong Wang, Ying Sun, Zhuopeng Wang, and Lin Shao*

College of Electronic and Information Engineering, Shandong University of Science and Technology, China

ABSTRACT: This paper presents a broadband circularly polarized (CP) implantable antenna for biomedical applications operating in the 2.45 GHz Industrial, Scientific, and Medical (ISM) band. Its key innovation is an annular ground plane structure with a square open slot, which simultaneously broadens both impedance and axial ratio (AR) bandwidths. This achieves a wide effective bandwidth of 30.8% (2.17–2.96 GHz), demonstrating superior bandwidth compared to existing implantable CP antennas. The antenna employs an inverted S-shaped radiating patch, and by adjusting the position of the radiating branches, it can switch between left-hand circular polarization (LHCP) and right-hand circular polarization (RHCP). The simulated and measured results of the antenna show good agreement, and the SAR meets IEEE standards.

1. INTRODUCTION

With the rapid development of biomedical electronics, implantable medical devices are assuming an ever-growing significance in disease monitoring, diagnosis, and therapy [1]. Clinical medical systems, including continuous glucose monitors [2], wireless capsule endoscopes [3], and cardiac pacemakers [4], necessitate robust bidirectional in/ex vivo communication architectures, where antenna characteristics predominantly dictate system reliability and clinical deployment feasibility [5]. However, the intricate electromagnetic characteristics of the human body present challenges for traditional implantable antennas, including bandwidth limitations, polarization mismatches, and the challenge of reconciling size with biocompatibility. Therefore, the development of a novel antenna design with wideband operation, CP, and in-body environment compatibility is urgently needed.

Communication with implantable medical devices faces the challenges of signal attenuation and frequency offset. Broadband antenna technology improves signal transmission robustness by extending the frequency domain and dynamically matching dielectric property changes [6]. In [7, 8], the bandwidth of the antenna is broadened by constructing the electromagnetic field superposition effect of multiple resonant modes. In [9], the effective path of the current is extended by loading four C-shaped open slots, thereby achieving miniaturization and broadband performance of the antenna. Notably, the introduction of metamaterial (MTM) technology opens up a new dimension for antenna design. In [10], the CP bandwidth is enhanced by integrating MTM structures with ε-extremely large properties on the antenna's cover layer. These innovations provide important solutions for reliable communication in implantable medical devices.

CP technology has become a key technology for solving the problem of complex electromagnetic environments in the human body and the mobility of implanted devices by its resistance to polarization mismatch and dynamic adaptation capability [11]. In [12–14], CP is achieved via various slot structure designs, including symmetric L-shaped slots, asymmetric T-shaped slots, and rectangular slots of varying lengths. In [15], improved diagonal cross-square-ring radiators are proposed to form directional current perturbations using cross single-arm splitting to achieve CP radiation. In [16], a wide-beam CP implantable antenna is designed by loading complementary open-ring resonators and C-shaped slots on the radiating patch. These innovative configurations enhance the stability and signal transmission reliability of implantable antennas in complex bioelectromagnetic environments. However, these designs still face challenges such as bulky dimensions, limited operational bandwidth, and suboptimal gain characteristics.

In this paper, a compact broadband CP implantable antenna operating within the 2.45 GHz ISM band is developed. The proposed antenna is made up of a radiating patch, ground, substrate, and superstrate and is characterized by a low profile and simple geometry. An inverted S-shaped radiator design fed by a coplanar waveguide (CPW), which excites orthogonal phase differences, produces the CP. The square open slot structure of the ground plane extends the antenna bandwidth through adjusting the current distribution. Electromagnetic simulations employ a single-layered-muscle, single-layered-skin, and three-layered phantom, demonstrating robust adaptability to biological tissues. Specific absorption rate (SAR) and link budget analyses confirm compliance with both biosafety standards and communication requirements.

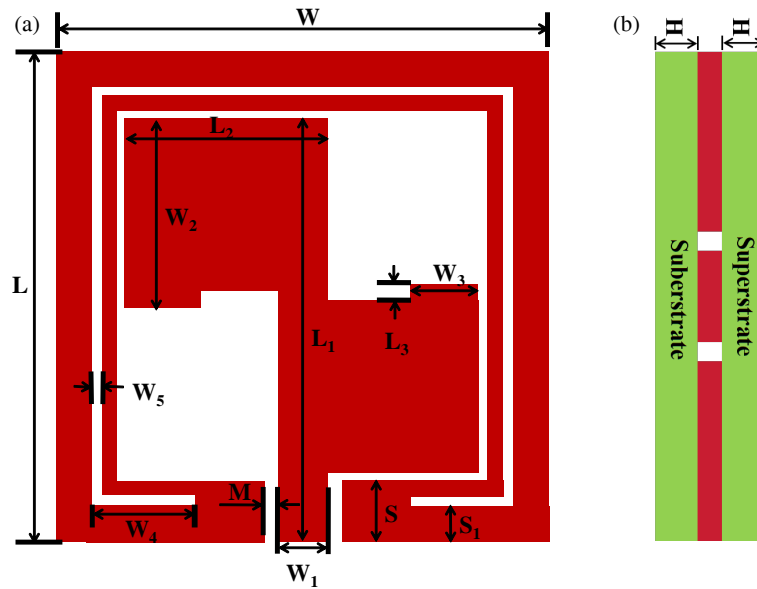* Corresponding author: Lin Shao (linshao@sdust.edu.cn).

FIGURE 1. Geometrical shape of proposed antenna. (a) Top view. (b) Side view.

2. DESIGN OF PROPOSED ANTENNA

2.1. Geometry of the Antenna

The antenna model is displayed in Fig. 1, using a substrate made of Rogers 3010 ($\varepsilon_r = 10.2$, $\tan \delta = 0.0035$) with 0.254 mm thickness. The superstrate shares identical material and geometric parameters with the underlying substrate, which ensures biosafety while building a stable dielectric environment. The radiator adopts an inverted S-shaped structure, which excites orthogonal current modes through geometrical asymmetry, thus generating RHCP properties. A square open slot is incorporated into the ground plane, and the impedance and AR bandwidths of the antenna are improved by adjusting the size and position of the slot to extend the surface current path. In addition, CPW feed method is adopted, and the ground-to-feedline gap is optimized to 0.3 mm to match 50 Ω impedance. Table 1 displays the specific parameters of the proposed antenna geometry.

TABLE 1. Geometrical parameters of the proposed antenna.

Parameters	Values/mm	Parameters	Values/mm
L	10	L_2	3.1
W	10	W_2	3.8
M	0.3	L_3	0.3
S	1.2	W_3	1.4
S_1	0.7	W_4	2.1
L_1	8.6	W_5	0.2
W_1	1	H	0.254

Since the proposed antenna operates within biological tissues, we need to consider its operating environment. In this design, a single-layered-muscle phantom is constructed to simulate the real biological environment. As illustrated in Fig. 2, the simulated environment measures $60 \times 60 \times 20$ mm³, with the muscle phantom exhibiting a relative permittivity of 52.73 and conductivity of 1.74 S/m at 2.45 GHz, respectively [17]. The
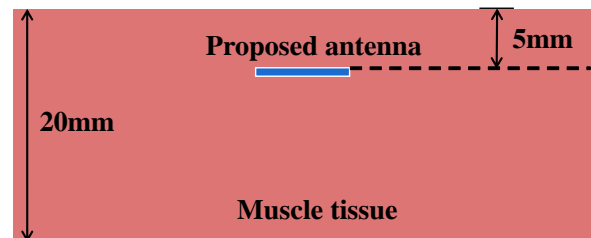

FIGURE 2. Simulation phantom of the proposed antenna.

proposed antenna is implanted 5 mm deep in the middle of the single-layered-muscle phantom.

2.2. Antenna Design

Since CPW feeding technology has a simple structure, wide bandwidth, low loss, and high anti-interference ability, it not only effectively realizes the antenna's low-profile and wide-bandwidth characteristics but also guarantees high-quality signal transmission and stable communication performance.

The length of a monopole antenna in a medium can be calculated using the following formula [18]:

$$L = \frac{c}{4 \times f \sqrt{\varepsilon_{\mathit{eff}}}} \tag{1}$$

where c is the speed of light, $\varepsilon_{\mathit{eff}}$ the effective permittivity constant of the medium, and f the operating frequency.

For this design, the operating environment is a mixed medium of superstrate and muscle tissue, and the effective permittivity constant $\varepsilon_{\mathit{eff}}$ can be calculated using the Lichtenecker formula [19]:

$$\ln(\varepsilon_{\mathit{eff}}) = v_2 \ln(\varepsilon_1) + v_1 \ln(\varepsilon_2) \tag{2}$$

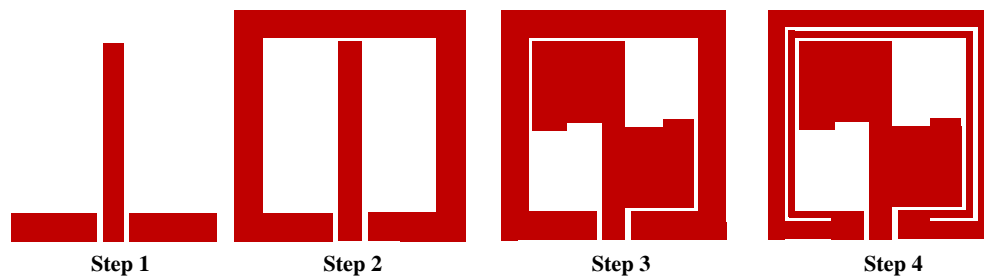**Step 1** **Step 2** **Step 3** **Step 4**

FIGURE 3. Evolution diagram of the proposed antenna.
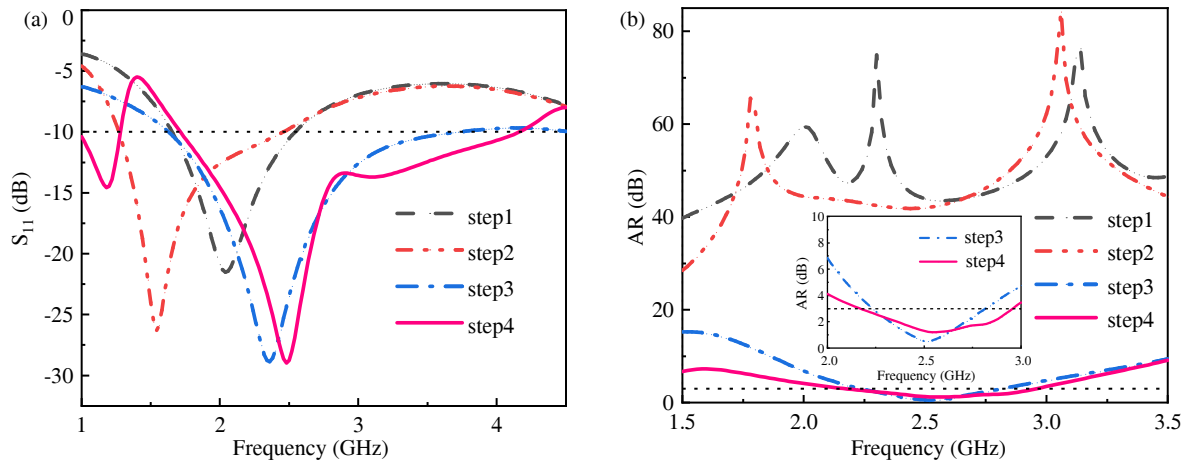
FIGURE 4. Simulation results for the four steps in S_{11} and AR. (a) S_{11}. (b) AR.

where ε_1 and ε_2 are the relative permittivity of the superstrate and muscle tissue; v_1 and v_2 are the volume percentages of the superstrate and muscle tissue, respectively.

The design steps of the proposed antenna are shown in Fig. 3.

Step 1: A conventional symmetric CPW-fed monopole antenna is designed considering biocompatibility and communication reliability.

Step 2: The ground plane is modified to an annular configuration, and its extension structure is utilized to expand the capacitive coupling area between the ground plane and radiating area, thus enhancing the electric field strength. This optimization strategy not only effectively extends the impedance bandwidth of the antenna but also improves the antenna gain and overall radiation performance by enhancing the energy coupling efficiency of the radiating surface.

Step 3: Two identical L-shaped branches are engineered to form an inverted S-shaped radiating structure. The structure introduces a 90° phase difference through geometric asymmetry, thereby achieving spatial and phase orthogonality of electromagnetic waves and realizing CP radiation while preserving amplitude balance.

Step 4: Introduce a square open slot in the ground to perturb the current distribution so that the ground current goes around along the edge of the square open slot, extending the current path and enhancing the impedance bandwidth and AR bandwidths.

The S_{11} and AR curves in Fig. 4 demonstrate the evolution of the impedance and CP during the design process, highlighting

the importance of the inverted S-shaped radiating structure to form the CP and square open slots to enhance the bandwidth.

3. RESULTS AND DISCUSSION

3.1. CP Radiating Mechanism

To better illustrate the operating principle of the antenna, Fig. 5 displays the surface current profiles of the antenna from 0° to 270° at 2.45 GHz. By observing the surface current distribution at four distinct time phases, it is evident that the primary current on the patch rotates counterclockwise, demonstrating that the proposed antenna achieves RHCP characteristics.

The RHCP characteristics are validated through the simulated radiation pattern in Fig. 6, where the antenna achieves a maximum gain of -24 dBi. Due to size limitations and the loss caused by surrounding human tissues, this antenna has low gain and is suitable for short-range communication, meeting the requirements of implantable medical devices. Cross-polarization discrimination of 19.84 dB for RHCP in the main radiation direction, thus showing high rejection of LHCP, and polarization purity meets medical band communication needs.

3.2. Parametric Analysis

Parametric studies reveal that the inverted S-shaped radiator's branch length L_3 and square open slot width W_5 critically influence impedance and CP, so L_3 and W_5 are parametrically analyzed to observe the performance changes. Fig. 7 displays
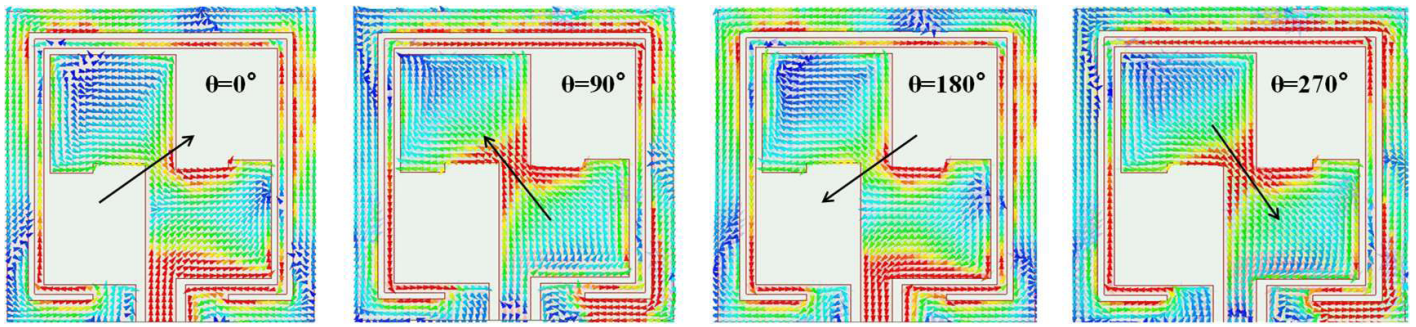
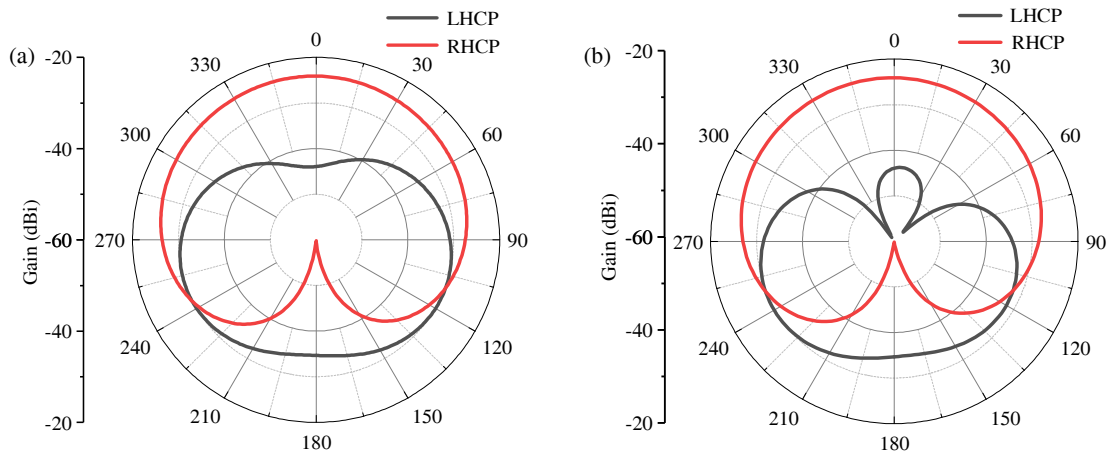**FIGURE 5**. Current distributions of the proposed antenna.

FIGURE 6. Simulated radiation patterns of LHCP and RHCP. (a) xoz-plane. (b) yoz-plane.
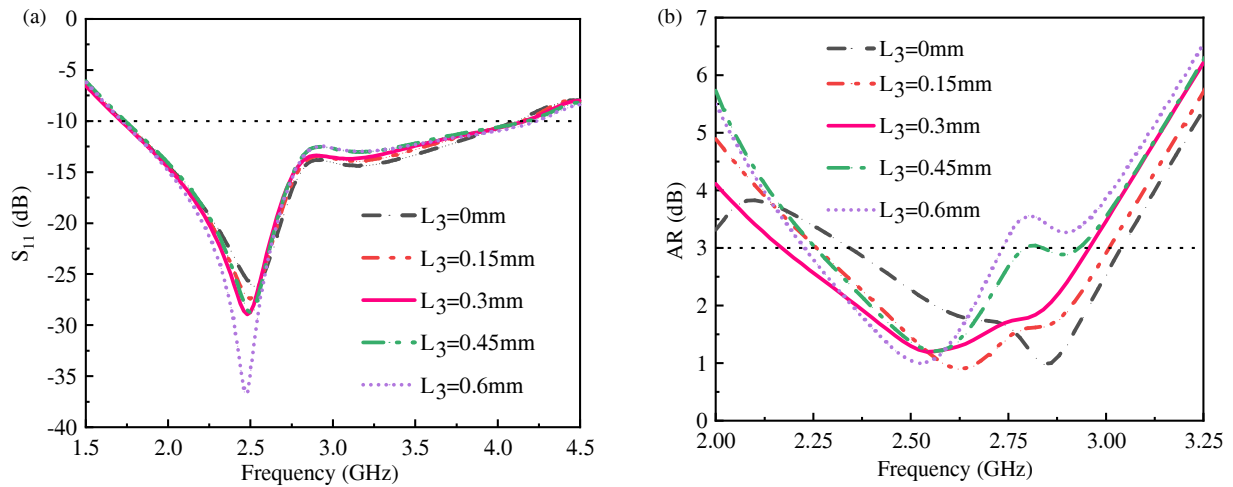

FIGURE 7. Impact of different parameters L_3 on the proposed antennas. (a) S_{11}. (b) AR.

the analysis of the length L_3 of the inverted S-shaped radiator's branches. As L_3 increases, the frequency is shifted to lower frequencies; the impedance bandwidth does not change significantly; and the AR bandwidth changes more significantly. When L_3 is 0.3 mm, the AR bandwidth is the widest, so $L_3 = 0.3$ mm is chosen. The effect of the width W_5 of the square open slot on impedance and CP is shown in Fig. 8. As

W_5 increases, both impedance bandwidth and AR bandwidth decrease, so $W_5 = 0.2$ mm is chosen.

3.3. Effect of Different Human Tissues

The proposed antenna is initially evaluated in a single-layered-muscle phantom. However, the heterogeneity of biological tissues and their electromagnetic property variations influence
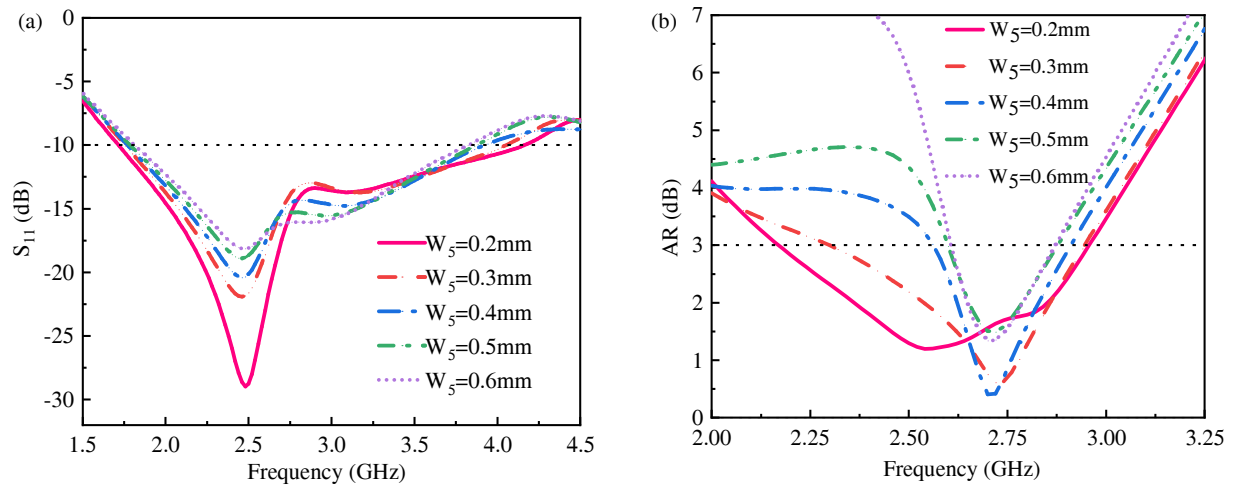
FIGURE 8. Impact of different parameters W_5 on the proposed antennas. (a) S_{11}. (b) AR.
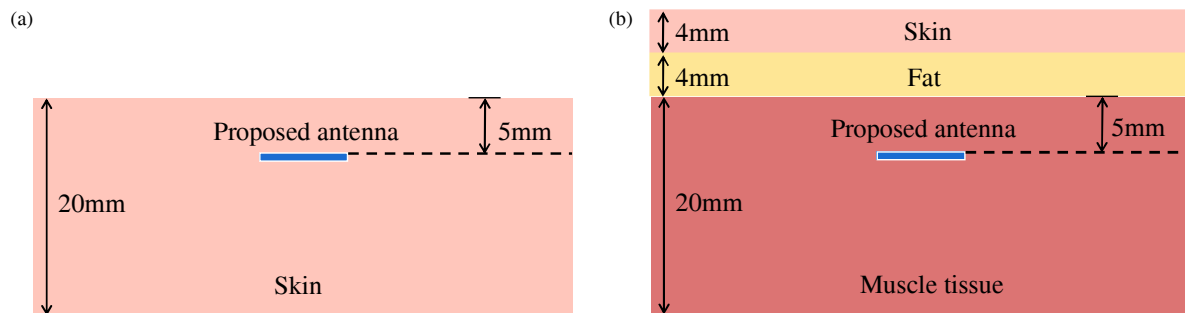

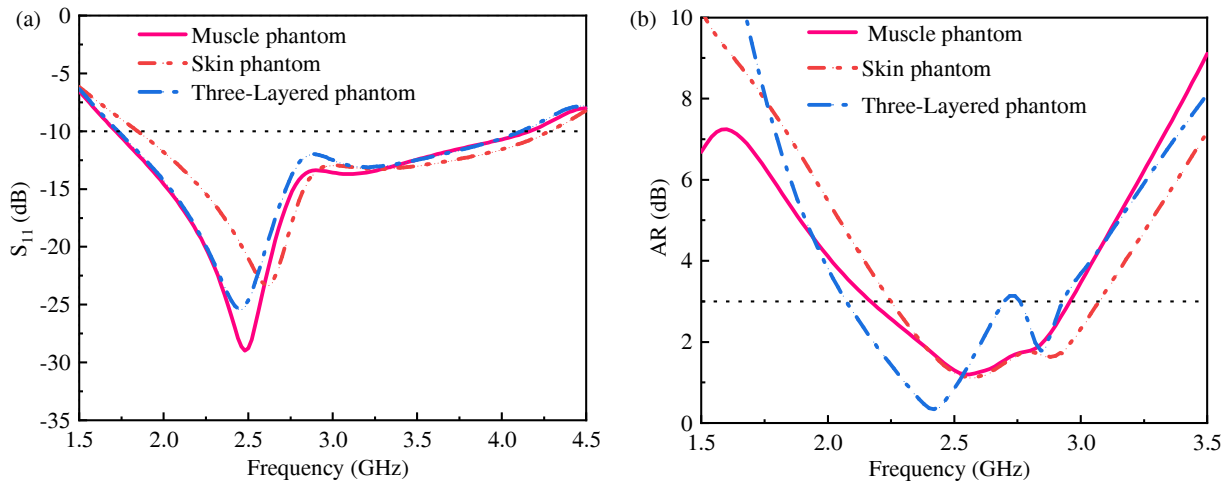**FIGURE 9**. Different body phantoms. (a) Skin phantom. (b) Three-layered phantom.

FIGURE 10. Simulation results of S_{11} and AR in different phantoms. (a) S_{11}. (b)AR.

both impedance and CP. In particular, the CP exhibits sensitivity to tissue phantom parameter variations. Therefore, the proposed antenna is implanted into different human body phantoms in Fig. 9, and Fig. 10 displays its S_{11} and AR variation curves. As illustrated in Fig. 10, when the antenna is embedded in a single layer of skin, the resonant frequency shifts upward because of the lower relative permittivity of skin than mus-

cle. When the antenna is embedded in a three-layered phantom, some detuning can be observed due to the complex tissue environment. Although the antenna has some differences in S_{11} and AR in different organization phantoms, the antenna is still able to cover the 2.45 GHz ISM band, and it has good stability.

Considering the clinical application requirements of implantable antennas, it is necessary to use biocompatible encap-
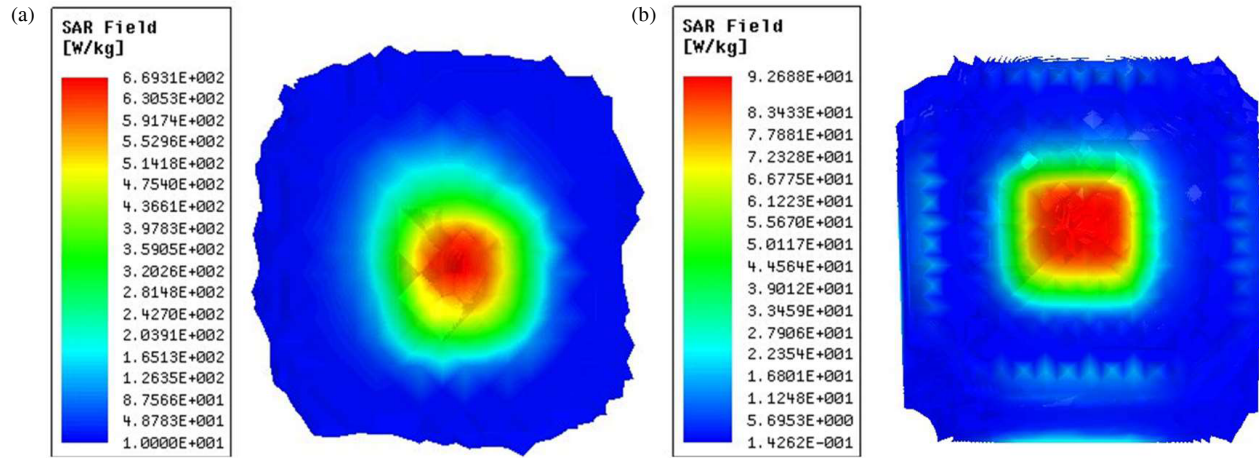
FIGURE 11. Simulated SAR distribution in the muscle phantom at 2.45 GHz. (a) 1 g SAR. (b) 10 g SAR.

3.4. SAR Analysis

The electromagnetic safety of the implanted antenna is analyzed. As shown in Fig. 11, the SAR values for the 1 g and 10 g standards at 2.45 GHz are 669.31 W/kg and 92.69 W/kg, respectively. According to the IEEE C95.1-2019 and IEEE C95.1-2005 standards, the calculated power limits of the antenna are 2.39 mW and 21.58 mW [20]. The actual operating input power is typically in the order of 100 μW, which is significantly lower than the maximum allowable power limits calculated above [21]. Therefore, the antenna meets the SAR safety requirements specified by the IEEE C95.1 standard at its intended operating power level.

3.5. Link Budget Analysis

To ensure reliable transmission of biomedical signals between implantable medical devices and external base stations, an accurate assessment of the communication coverage is a key prerequisite for guaranteeing reliable transmission of biological information. To determine the maximum effective communication range under in vivo operating conditions, link margin analysis employs the following equation [21]:

$$\text{Link margin (dB)} = \text{Link}\frac{C}{N_0} - \text{Required}\frac{C}{N_0} \quad (3)$$

$$LM\,(\text{dB}) = (P_t + G_t - L_f + G_r - N_0)$$
$$- \left(\frac{E_b}{N_0} + 10\log_{10} B_r - G_c + G_d\right) \quad (4)$$

$$L_f\,(\text{dB}) = 20\log_{10}\left(\frac{4\pi d}{\lambda}\right) \quad (5)$$

where P_t is the transmitted power, G_t the transmitting antenna gain, L_f the free space path loss, G_r the receiving antenna gain, N_0 the noise power density, and B_r the bit rate.

TABLE 2. Communication link margin-related parameters.

Central Frequency (GHz)	2.45
Transmitted power, P_t (dBW)	−40
T_x antenna gain, G_t (dBc)	−24
R_x antenna gain, G_r (dBi)	2.15
Noise power density, N_0 (dB/Hz)	−199.95
E_b/N_0 (ideal PSK) (dB)	9.6
Coding gain, G_c (dB)	0
Fixing deterioration, G_d (dB)	2.5
Bit rate, Br (Kbps)	10,100,1000

Applying the above equations and the relevant parameters in Table 2, the link margins at three data rates are computed. Polarization mismatch loss and impedance loss are ignored for the ease of calculation, but a 20 dB link margin is incorporated to ensure communication reliability. From Fig. 12, it can be observed that the maximum transmission distance is 19.44, 6.15, and 1.94 m for bit rates of 10 Kbps, 100 Kbps, and 1 Mbps, respectively. The proposed antenna can maintain a good communication distance.
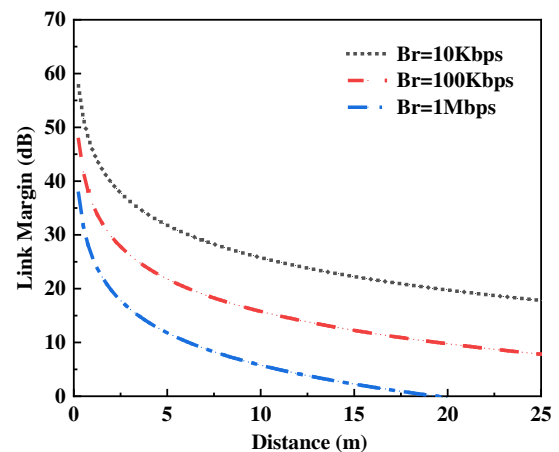

FIGURE 12. Link margin analysis for telemetry range at different data rates.

TABLE 3. Comparison of reported and proposed antenna performance.

Ref.	Freq (GHz)	I-BW (%)	AR-BW (%)	Gain (dBi)	$SAR_{1g,max}$ (W/kg)	Volume (mm^3)
[9]	2.4	30.4%	16.9%	−32.8	—	71.4
[10]	0.915	17.8%	21.3%	−17.1	576.1	21.34
	2.45	35.8%	17.14%	−9.81	524.3	
[12]	2.4	16.13%	22.22%	−37.36	856.45	63.8
[13]	2.45	46.5%	23.6%	−28.8	652.3	17.78
[14]	2.4	6.2%	8.13%	−27.2	—	127
[15]	2.45	30.0%	28.7%	−24.7	697.5	85.38
Proposed antenna	2.45	82.99%	30.8%	−24	669.31	50.8
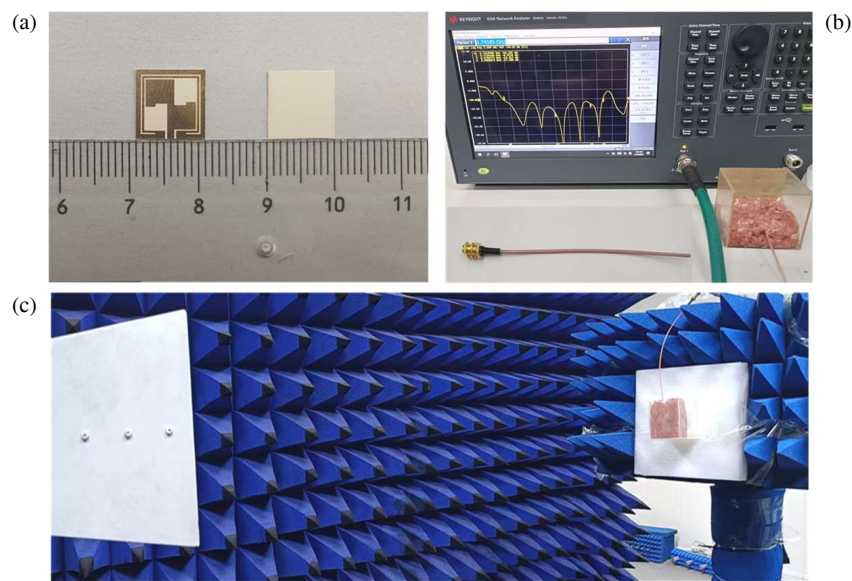
FIGURE 13. Antenna prototype and measurement device. (a) Antenna prototype. (b) Return loss measurement device. (c) Far-field measurement device.

4. MEASUREMENT RESULTS ANALYSIS

To verify operational performance, the antenna prototype is made and measured as illustrated in Fig. 13. The S_{11} of the antenna is measured using a vector network analyzer (VNA), and then the far-field radiation characteristics of the antenna are evaluated in an anechoic chamber.

The measured and simulated results of the antenna S_{11} are shown in Fig. 14(a). The results show that when the antenna is embedded in minced pork, the measured −10 dB impedance bandwidth obtained is 3090 MHz (95.5%), and the effective operating band covers 1.69–4.78 GHz, which is a slightly increased bandwidth compared to the simulated results. It is worth noticing that five resonance points appear in the measured S_{11} curve, while there is only one resonance point in the simulated S_{11}. A similar phenomenon has been observed in the literature [22, 23]. The cause of this phenomenon stems from the synergistic effects of multiple factors: (1) interface discontinuities formed by minute air gaps between the antenna and tissue lead to multiple reflections and scattering; (2) ideal port simulations do not account for the parasitic effects of SMA connectors and cables; (3) inherent tissue heterogeneity causes spatial variations in dielectric parameters; (4) infiltrated bodily fluids alter the local electromagnetic environment and introduce coupling paths; (5) manufacturing tolerances affect resonant characteristics. Fig. 14(b) shows the measurement and simulation results of the 3 dB AR bandwidth of the antenna, which is measured in minced pork at 890 MHz (33.4%) with an effective operating band covering 2.22–3.11 GHz. The measurements are slightly offset compared to the simulation results. This effect may be due to the difference between the simulation and measurement environments.

Table 3 provides a comparison of the proposed antenna with the reported antennas, and the results show that the proposed antenna has a smaller size, wider impedance bandwidth and AR bandwidth, and higher gain.
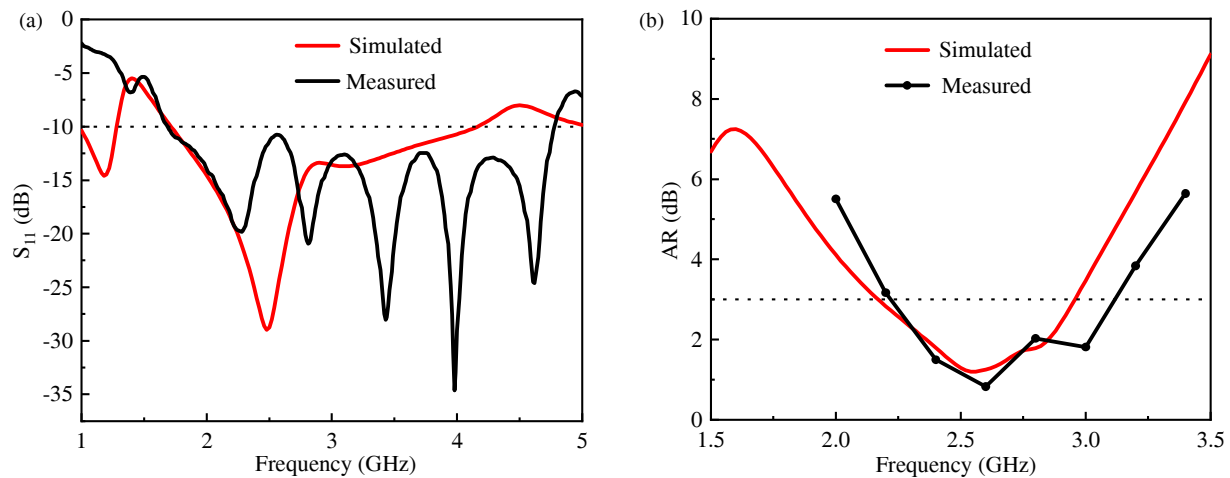
FIGURE 14. Simulated (muscle phantom) and measured (a) S_{11}, (b) AR.

5. CONCLUSION

This paper presents a broadband CP implantable antenna for the 2.45 GHz ISM band. Based on an innovative structural design combining an inverted S-shaped radiator with a square slot on the ground plane, this antenna achieves CP and broadband matching characteristics. Experimental results indicate that the antenna exhibits good impedance and AR bandwidths, meets human body SAR safety regulations, and possesses strong wireless communication capabilities. These characteristics demonstrate good potential for application in implantable biomedical devices.

REFERENCES

[1] Mohan, A. and N. Kumar, "Implantable antennas for biomedical applications: A systematic review," *BioMedical Engineering OnLine*, Vol. 23, No. 1, 87, 2024.

[2] Karacolak, T., A. Z. Hood, and E. Topsakal, "Design of a dual-band implantable antenna and development of skin mimicking gels for continuous glucose monitoring," *IEEE Transactions on Microwave Theory and Techniques*, Vol. 56, No. 4, 1001–1008, Apr. 2008.

[3] Song, Z., X. Xu, Y. Shi, and L. Wang, "Design of a compact circularly polarized implantable antenna for capsule endoscopy systems," *Sensors*, Vol. 24, No. 12, 3960, 2024.

[4] Lamkaddem, A., A. E. Yousfi, K. A. Abdalmalak, V. G. Posadas, and D. Segovia-Vargas, "Circularly polarized miniaturized implantable antenna for leadless pacemaker devices," *IEEE Transactions on Antennas and Propagation*, Vol. 70, No. 8, 6423–6432, Aug. 2022.

[5] Xia, Z., H. Li, Z. Lee, S. Xiao, W. Shao, X. Ding, *et al.*, "A wideband circularly polarized implantable patch antenna for ISM band biomedical applications," *IEEE Transactions on Antennas and Propagation*, Vol. 68, No. 3, 2399–2404, Mar. 2020.

[6] Wang, M., H. Liu, P. Zhang, X. Zhang, H. Yang, G. Zhou, and L. Li, "Broadband implantable antenna for wireless power transfer in cardiac pacemaker applications," *IEEE Journal of Electromagnetics, RF and Microwaves in Medicine and Biology*, Vol. 5, No. 1, 2–8, Mar. 2021.

[7] Yousaf, M., I. B. Mabrouk, M. Zada, A. Akram, Y. Amin, M. Nedil, and H. Yoo, "An ultra-miniaturized antenna with ultra-wide bandwidth characteristics for medical implant systems," *IEEE Access*, Vol. 9, 40 086–40 097, 2021.

[8] Song, Z. and M. Li, "Ultra-wideband circular polarized implantable patch antenna for implantable blood glucose detection system applications," *Sensors*, Vol. 24, No. 16, 5292, 2024.

[9] Xu, C., Y. Fan, and X. Liu, "A circularly polarized implantable rectenna for microwave wireless power transfer," *Micromachines*, Vol. 13, No. 1, 121, 2022.

[10] Zada, M., I. A. Shah, and H. Yoo, "Metamaterial-loaded compact high-gain dual-band circularly polarized implantable antenna system for multiple biomedical applications," *IEEE Transactions on Antennas and Propagation*, Vol. 68, No. 2, 1140–1144, Feb. 2020.

[11] Yang, Z.-J., L. Zhu, and S. Xiao, "An implantable circularly polarized patch antenna design for pacemaker monitoring based on quality factor analysis," *IEEE Transactions on Antennas and Propagation*, Vol. 66, No. 10, 5180–5192, Oct. 2018.

[12] Liu, R., K. Zhang, Z. Li, W. Cui, W. Liang, M. Wang, C. Fan, H. Zheng, and E. Li, "A wideband circular polarization implantable antenna for health monitor microsystem," *IEEE Antennas and Wireless Propagation Letters*, Vol. 20, No. 5, 848–852, May 2021.

[13] Song, Z., X. Zheng, Y. Shi, and Y. Wang, "Implantable small ultra-wideband circularly polarized antenna design for continuous blood pressure monitoring," *Scientific Reports*, Vol. 14, No. 1, 25199, 2024.

[14] Yang, Z.-J., S.-Q. Xiao, L. Zhu, B.-Z. Wang, and H.-L. Tu, "A circularly polarized implantable antenna for 2.4-GHz ISM band biomedical applications," *IEEE Antennas and Wireless Propagation Letters*, Vol. 16, 2554–2557, 2017.

[15] Jing, D., H. Li, X. Ding, W. Shao, and S. Xiao, "Compact and broadband circularly polarized implantable antenna for wireless implantable medical devices," *IEEE Antennas and Wireless Propagation Letters*, Vol. 22, No. 6, 1236–1240, Jun. 2023.

[16] Liu, X. Y., Z. T. Wu, Y. Fan, and E. M. Tentzeris, "A miniaturized CSRR loaded wide-beamwidth circularly polarized implantable antenna for subcutaneous real-time glucose monitoring," *IEEE Antennas and Wireless Propagation Letters*, Vol. 16, 577–580, 2017.

[17] Gabriel, C., S. Gabriel, and E. Corthout, "The dielectric properties of biological tissues: I. Literature survey," *Physics in Medicine & Biology*, Vol. 41, No. 11, 2231, 1996.

[18] Abbosh, A. M. and M. E. Bialkowski, "Design of ultrawideband planar monopole antennas of circular and elliptical shape," *IEEE Transactions on Antennas and Propagation*, Vol. 56, No. 1, 17–23, Jan. 2008.

[19] Lichtenecker, K., "Die herlritung des logarithmischen mischungsgesetzes aus allgemeinen prinzipien der stationaren stromung," *Phys. Z*, Vol. 32, 255–260, 1931.

[20] Shah, S. A. A. and H. Yoo, "Scalp-implantable antenna systems for intracranial pressure monitoring," *IEEE Transactions on Antennas and Propagation*, Vol. 66, No. 4, 2170–2173, Apr. 2018.

[21] Rajagopalan, H. and Y. Rahmat-Samii, "Wireless medical telemetry characterization for ingestible capsule antenna designs," *IEEE Antennas and Wireless Propagation Letters*, Vol. 11, 1679–1682, 2012.

[22] Mishra, P. K. and V. S. Tripathi, "A miniature dielectric loaded wide band circularly polarized implantable antenna with low specific absorption rate for biomedical applications," *International Journal of RF and Microwave Computer-Aided Engineering*, Vol. 32, No. 8, e23227, 2022.

[23] Shang, J. and Y. Yu, "An ultrawideband capsule antenna for biomedical applications," *IEEE Antennas and Wireless Propagation Letters*, Vol. 18, No. 12, 2548–2551, 2019.

[24] Kaim, V., B. K. Kanaujia, S. Kumar, H. C. Choi, K. W. Kim, and K. Rambabu, "Ultra-miniature circularly polarized CPW-fed implantable antenna design and its validation for biotelemetry applications," *Scientific Reports*, Vol. 10, No. 1, 6795, 2020.